IEEE Access
Multidisciplinary | Rapid Review | Open Access Journal

Received March 18, 2019, accepted April 22, 2019, date of publication May 8, 2019, date of current version July 1, 2019.

Digital Object Identifier 10.1109/ACCESS.2019.2915530

Electrical Capacitance Tomography Using Incomplete Measurement Set

ZIQIANG CUI, (Member, IEEE), ZIHAN XIA, AND HUAXIANG WANG, (Senior Member, IEEE)
School of Electrical and Information Engineering, Tianjin University, Tianjin 300072, China

Corresponding author: Ziqiang Cui (cuiziqiang@tju.edu.cn)

This work was supported by the National Natural Science Foundation of China under Grant 61671319 and Grant 61627803.

ABSTRACT In the electrical capacitance tomography (ECT) systems, the electrodes, and cables may fail to function properly, which will cause several measurements missing. In these cases, image reconstruction can only use the remaining effective measurements. In order to make the reconstructed images close to the image results of the complete measurement set, it is necessary to use the incomplete measurements reasonably. The measurement/data recovery method and image reconstruction can be conducted to obtain the results, which meet the imaging needs under these circumstances. The measurement/data recovery method by using the sensitivity matrix and the regression model of least square support vector machine (LS-SVM) are proposed. The image recovery result is reconstructed by the method of total variation (TV) minimization. The simulations and experiments of gas–solids two-phase measurement are conducted to validate the method.

INDEX TERMS Electrical capacitance tomography (ECT), incomplete measurement set, image reconstruction, measurement/data recovery.

I. INTRODUCTION

Electrical capacitance tomography (ECT) is an online imaging tool that utilizes the inter-electrode capacitance measurements to estimate the cross-sectional dielectric distributions by using a proper image reconstruction algorithm. Being inexpensive, non-intrusive and non-radioactive, ECT technique is suitable for imaging the industrial processes, in which fast-going multi-phase flow is frequently met. The applications of ECT can be found in the circulating fluidized bed [1]–[3], trickle-bed reactor, temperature measurement [4], flame detection [5], [6] and multi-phase flow rate measurement [7], [8].

Generally, the ECT sensor consists of a circular electrode array that placed on the periphery of vessel/pipe cross-sectional, which is usually non-invasive and non-intrusive to the investigated flows and pipes. The number of electrode on a sensor plane can be 8, 12 or 16. For a n-electrode ECT sensor, there exists m independent measurements, *i.e.* $m = n(n-1)/2$. The m capacitance measurements constitute the complete measurement set, which contains all the inter-electrode capacitances. The inverse problem is to calculate the dielectric distribution from the capacitance measurement set.

The associate editor coordinating the review of this manuscript and approving it for publication was Eduardo Rosa-Molinar.

In some cases, however, the measurement failures may occur and cannot be handled in time, *i.e.* due to the measuring circuits, electrodes and signal cables. This will lead to the incomplete measurement sets, in which the number of effective measurements is smaller than the complete measurement sets, *i.e.* $m' < m$. In this case, the reconstructed images may be seriously affected.

This can be solved at the different levels, *i.e.* by measurement/data or image recovery method. It is suggested that the regression and the expectation maximization (EM) methods are suitable for handling the problem of missing measurement/data [9]. The missing and remaining measurements are related in the temporal and spatial aspects, therefore the regression model can be set up by using the artificial intelligent algorithm, *e.g.* neural network and support vector regression. If there existed a certain probability distribution in the measurements/data, the Bayesian networks and EM methods can been applied to recover the missing data [9]–[11]. In the ECT measurements, if the measured phase distribution changes frequently, the statistical characteristics are difficult to attain. Therefore, the regression method is more appropriate for the measurement/data recovery in ECT.

In this paper, a measurement/data recovery method in combination with TV minimization algorithm has been proposed to deal with the problem of incomplete measurement.

The performance of method has been evaluated with simulations as well as experiments.

II. METHOD

A. PROBLEM DEFINITION

The complete measurement set contains m independent measurements, which can be expressed as a measurement matrix, *i.e.*

$$\mathbf{C} = \{C_{j,k}\}, \quad j,k \in \{1,2,\cdots,n\},\ j \neq k. \tag{1}$$

where $C_{j,k}$ indicates the inter-electrode capacitance between electrodes j and k. Note that the measurements refer to the normalized capacitances. In consideration of the reciprocal theory, *i.e.* $C_{j,k} = C_{k,j}$, the number of elements in $\mathbf{C}$ can be reduced by 1/2, which results in $m = n(n-1)/2$.

Assume that the failures occur in the measurement channel/electrode i, where $i \in \{1,2,\cdots,n\}$, the measurement set becomes incomplete, *i.e.*

$$\widetilde{\mathbf{C}} = \{C_{j,k}\}, \quad j,k \in \{1,2,\cdots,n\} \setminus \{i\},\ j \neq k. \tag{2}$$

Fig. 1 illustrates the image reconstruction result of a 12-electrode ECT sensor with and without its electrode 1. Fig.1(a) is the tested phantom. Fig.1(b) presents the image that reconstructed from the complete measurement set, while Fig. 1(c) shows the image that reconstructed from the incomplete measurement set, *i.e.* without the electrode E_1. In this case, the number of measurements is reduced from 66 to 55.

TABLE 1. Nomenclature.

Variables	Description
n	The number of electrodes in an ECT sensor plane
m	The number of measurements in the complete measurement set
m'	The number of effective measurements in the incomplete measurement set
$\mathbf{C}$	The complete measurement set
$\widetilde{\mathbf{C}}$	The incomplete measurement set
$\mathbf{C_m}$	The missing measurements
$\widehat{\mathbf{C}}'$	The estimated complete measurement set of $\widetilde{\mathbf{C}}$ using the sensitivity matrix of ECT
$\widehat{\mathbf{C_r}}$	$\widehat{\mathbf{C}}'$ for training input of regression models
$\widehat{\mathbf{C_e}}$	$\widehat{\mathbf{C}}'$ for testing input of regression models
$\widehat{\mathbf{C_m}}$	The recovered missing measurements
$\widehat{\mathbf{C}}$	The recovered measurement set of $\widetilde{\mathbf{C}}$
$\mathbf{C_r}$	The training sample consists of the corresponding $\mathbf{C_m}$ and $\widehat{\mathbf{C_r}}$
$\mathbf{C_r^*}$, $\mathbf{C_e^*}$	The total training and test samples with labels
$\widetilde{\mathbf{g}}$	Image result of incomplete measurement set
$\widehat{\mathbf{g}}$	Image result of recovered measurement set
$\mathbf{g}$	Image result of complete measurement set

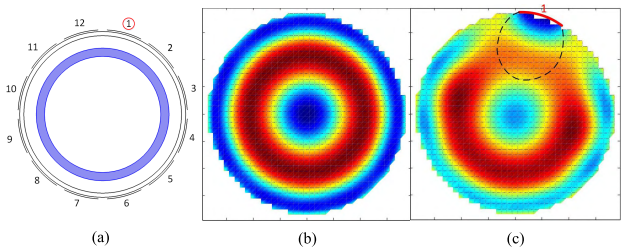

FIGURE 1. Image reconstruction results of (a) the tested phantom using (b) the complete measurement set, and (c) incomplete measurement set without E_1 related capacitances.

It can be seen that the image areas adjacent to the electrode 1 of incomplete measurement set are seriously distorted.

B. PREPROCESSING OF INCOMPLETE MEASUREMENT SET

To improve the quality of image that reconstructed from the incomplete measurement set, it is necessary to, 1) restore the measurement set as close to the complete measurement set as possible, and 2) employ a suitable image reconstruction algorithm that could tolerate or eliminate the errors that occurred in the data restoration process.

Note that the missing capacitances cannot be ideally recovered and the recovery errors will always exist. Therefore, it is necessary to apply a suitable image reconstruction algorithm with the capability of noise reduction.

In restoring the missing measurements, the incomplete measurements should close to its counterpart of complete measurement set to make sure the effectiveness of recovery method. The sensitivity matrix in ECT is defined as:

$$\mathbf{S}(\varepsilon) = \frac{dC(\varepsilon)}{d\varepsilon}|_{\varepsilon=\varepsilon_0} \tag{3}$$

In consideration that the sensitivity matrix contains the mutual information on different capacitance measurements, one may recover the missing measurements from the incomplete measurement set by solving the inverse and forward problems.

For the implementation, a reconstruction image is calculated from the incomplete measurement set with the linear-back projection algorithm, *i.e.*

$$\widetilde{\mathbf{g}} = \mathbf{S}_{ic}^{-1} \cdot \widetilde{\mathbf{C}} \tag{4}$$

where $\mathbf{S_{ic}^{-1}}$ is the pseudo inverse of sensitivity matrix that obtained for the incomplete measurement set. The matrix $\mathbf{S_{ic}}$ is constructed from the column vectors corresponding to the incomplete measurements.

Subsequently, a complete measurement set $\widehat{\mathbf{C}}'$ can be estimated from $\widetilde{\mathbf{g}}$:

$$\widehat{\mathbf{C}}' = \mathbf{S} \cdot \widetilde{\mathbf{g}} \tag{5}$$

where $\mathbf{S}$ is the sensitivity matrix of complete measurement set.

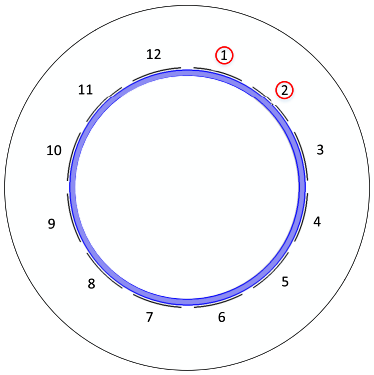

FIGURE 2. Simulation model of the 12 electrodes ECT.

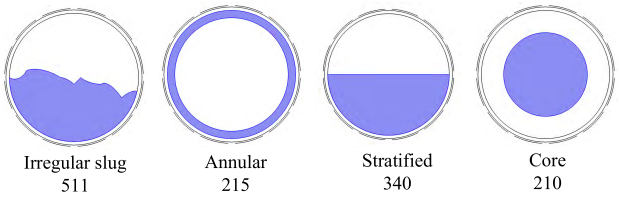

FIGURE 3. Typical distributions and number of measurement sets.

In this way, the mutual relationships offered by the sensitivity matrix between the incomplete measurements and missing measurements can be utilized. However, the error will always exist in the aforementioned process, which should be paid more attention to.

The quantity of effective measurements is increased by solving the inverse and forward problems, which is beneficial to fit the relationship between $\widehat{\mathbf{C}}'$ and $\mathbf{C_m}$. At this step, the recovered measurement set is further processed by regression model.

Prior to performing the regression method, the singular value decomposition (SVD) method is adopted to analyze the relationships between the measurement sets. As shown in Fig.2, a 12-electrode ECT has been applied to obtain the measurement sets in the simulations.

The measurement sets of gas-solid two-phase flows consist of 4 typical distributions (mimicking the cross-sectionals of irregular air slugs, annular flow, stratified flow and core flow which are frequently met in the pneumatic conveying processes [12], [13] and gas-solid fluidization [14]), as illustrated in Fig 3. Totally, 1276 measurement sets of the typical distributions are analyzed by the SVD method. The distributions contain irregular slug, annular, stratified and core with different shapes and levels of boundary, thicknesses of annular, heights of solid layer, diameters and positions of core. The shaded parts indicate the high permittivity material, Perspex particles in this case, and the background material is air.

Fig. 4(a) shows the singular value curve of measurement matrix. The curve slope is sharp at its beginning, indicating the linear dependencies between the measurements, while the relationship is nonlinear and changes with dielectric

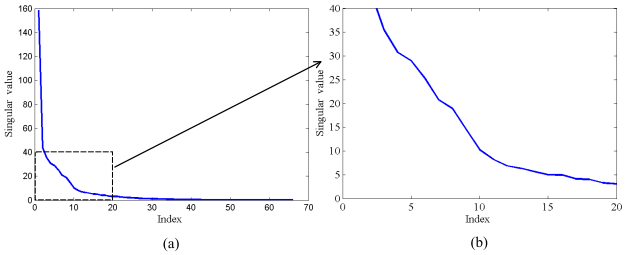

FIGURE 4. Singular value curve of total measurement samples: (a) complete curve and (b) local curve.

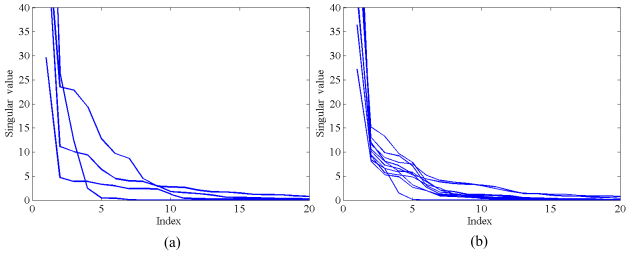

FIGURE 5. Local singular value curve of (a) samples in 4 categories classified by flow regimes, and (b) samples in 10 categories clustered by K-means.

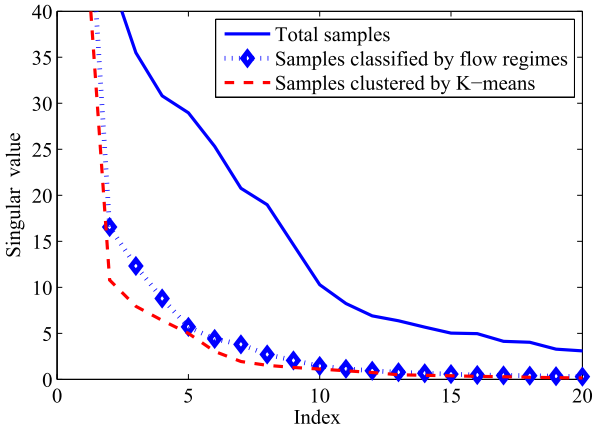

FIGURE 6. Comparison of mean value curve of singular value.

distribution. The fitting effect of regression model would be better if the relationships in data set is simple. The measurement samples can be classified or clustered into several categories to decrease the complexity of relationship, which can be conducted by implementing machine learning algorithms or by artificially classified flow regimes. Fig. 4(b) and Fig. 5(a, b) show the local singular value curve of total samples, samples in the 4 categories of different flow regimes (group 1) and samples in the 10 categories clustered by K-means algorithm (group 2). The total samples illustrated in each figures are of the same quantity, *i.e.* 1276. It can be discerned in these curves that the reduction speed in the singular value of total samples is obviously slower than samples in categories. Furthermore, the reduction speed of singular value in group 2 is more uniform than group 1. Fig. 6 shows that the comparison between singular value curve of total samples and mean singular value curves of group 1 and 2. The curve

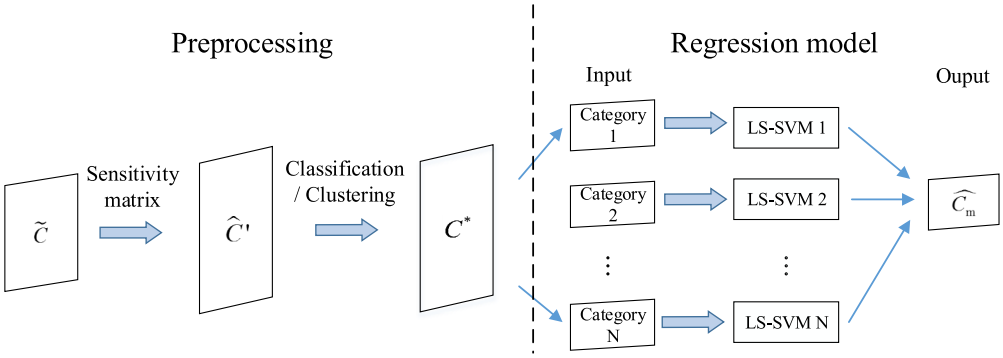

FIGURE 7. Measurement/data recovery method.

of samples clustered by K-means shows the fastest descent rate indicating the simplest relationships between measurements. Therefore, the samples in the categories clustered by K-means are used to train the regression models.

The K-means algorithm is able to minimize the sum of squared error between the empirical mean of clusters and the points in clusters. The sum of squared error over all K clusters is defined as:

$$\mathbf{J}(\mathbf{A}) = \sum_{i=1}^{K} \sum_{\widehat{\mathbf{C}_\mathbf{r}} \in \mathbf{A_i}} ||\mu_i - \widehat{\mathbf{C}_\mathbf{r}}||_2^2 \tag{6}$$

where $\mathbf{A_i}$ is the i-th cluster and μ_i is the mean value of it.

The main steps of the algorithm are as follows [15]:

1. Select an initial partition with K clusters; repeat steps 2 and 3 until cluster membership stabilizes.

2. Generate a new partition by assigning each pattern to its closest cluster center.

3. Compute new cluster centers.

In consideration of the relationship between $\widehat{\mathbf{C}_\mathbf{r}}$ and $\mathbf{C_r}$, it should be noted that the clustering result is obtained from $\widehat{\mathbf{C}_\mathbf{r}}$ and the acquired labels also corresponds to $\mathbf{C_r}$. Consequently, the labels of entire $\mathbf{C_r}$ are obtained forming labeled training samples $\mathbf{C_r}^*$. After the clustering, $\mathbf{C_r}^*$ forms K training sets according to the labels of samples.

Similarly, the test samples need to be classified, according to the clustering results, *i.e.* each test sample is categorized into the suitable categories. A test sample is classified according to its data characteristics which show the highest consistency with characteristics of training samples in category. The random forest (RF) method is used to classify the test samples, $\widehat{\mathbf{C}_\mathbf{e}}$, into the K categories, which can be expressed as:

$$\mathfrak{L}(e) = f(\widehat{\mathbf{C}_\mathbf{e}}, \mathbf{C_r}^*) \tag{7}$$

where $\widehat{\mathbf{C}_\mathbf{e}}$ is one of the test samples and $\mathfrak{L}(e)$ is its index.

The labeled test samples $\mathbf{C_e}^*$ can be obtained by classification and the labels correspond to the categories of regression models. Consequently, the test sets of regression models are obtained.

The classification/clustering strategy of samples contributes to utilizing the finite training samples effectively and reducing the calculation time significantly.

C. REGRESSION METHOD

The steps of measurement recovery using regression method is shown in Fig.7.

The LS-SVM technique provides a solution which allows recasting the convex nonlinear optimization problem for SVM regression [16], [17]:

$$\mathcal{M}_{SVM}(\mathbf{x}) = \langle \mathbf{w}, \Phi(\mathbf{x}) \rangle + b \tag{8}$$

where $\Phi = [\phi_1(\mathbf{x}), \ldots, \phi_D(\mathbf{x})]$ is a nonlinear map $\Phi(\cdot)$: $\mathbb{R}^d \rightarrow \mathbb{R}^D$ which maps the parameter space of dimension d into the corresponding feature space of dimension D; $\mathbf{w} \in \mathbb{R}^D$ is a vector collecting the unknown coefficients of the nonlinear regression; $b \in \mathbb{R}$ is the bias term; $\langle \mathbf{w}, \Phi(\mathbf{x}) \rangle$ is defined as the inner product in $\mathbb{R}^D$.

And the optimization problem is formulated as:

$$\begin{aligned} &\text{minimize } \frac{1}{2}\|\mathbf{w}\|^2 + \gamma \frac{1}{2} \sum_{i=1}^{L} e_i^2 \\ &\text{subject to } y_i = \langle \mathbf{w}, \Phi(\mathbf{x}_i) \rangle + b + e_i, \quad \text{for } i = 1, \ldots, L \end{aligned} \tag{9}$$

where $e_i \in \mathbb{R}$ is one of the error variables and γ is an empirical parameter which provides a trade-off between the accuracy of the model and its generalization ability.

The optimization object is to minimize the squares of the regression errors, e_i and at the same time, guarantee the generalization ability of regression model. The optimization problem can be solved by minimizing the Lagrangian:

$$\begin{aligned} \mathcal{L}(\mathbf{w}, b, \mathbf{e}; \alpha) = &\frac{1}{2}\|\mathbf{w}\|^2 + \gamma \frac{1}{2} \sum_{i=1}^{L} e_i^2 \\ &- \sum_{i=1}^{L} \alpha_i \{ \langle \mathbf{w}, \Phi(\mathbf{x}_i) \rangle + b + e_i - y_i \} \end{aligned} \tag{10}$$

where $\alpha_k \geq 0$ is one of the Lagrange multipliers.

It can be minimized by solving the following partial derivatives:

$$\begin{aligned}
&\frac{\partial \mathcal{L}}{\partial \mathbf{w}} = 0 \rightarrow \mathbf{w} = \sum_{i=1}^{L} \alpha_i \Phi(\mathbf{x}_i) \\
&\frac{\partial \mathcal{L}}{\partial b} = 0 \rightarrow \sum_{i=1}^{L} \alpha_i = 0 \\
&\frac{\partial \mathcal{L}}{\partial e_i} = 0 \rightarrow \alpha_i = \gamma e_i \\
&\frac{\partial \mathcal{L}}{\partial \alpha_k} = 0 \rightarrow \langle \mathbf{w}, \Phi(\mathbf{x}_i) \rangle + b + e_i - y_i = 0
\end{aligned} \tag{11}$$

By substituting the first three equations into the above equation, the dual space equations can be obtained [18]:

$$\begin{cases}
\sum_{i=1}^{L} \alpha_i = 0 \\
\sum_{i=1}^{L} \alpha_i K(\mathbf{x}_i, \mathbf{x}_1) + b + \gamma \alpha_1 - y_1 = 0 \\
\vdots \\
\sum_{i=1}^{L} \alpha_i K(\mathbf{x}_i, \mathbf{x}_L) + b + \gamma \alpha_L - y_L = 0
\end{cases} \tag{12}$$

where $K(\mathbf{x}_i, \mathbf{x}_j) = \left\langle \Phi(\mathbf{x}_i), \Phi(\mathbf{x}_j) \right\rangle$ is the kernel function defined for the case of regression.

The equation can be expressed in matrix form,

$$\begin{bmatrix} 0 & \mathbf{1}^T \\ \mathbf{1} & \Omega + \mathbf{I}/\gamma \end{bmatrix} \begin{bmatrix} b \\ \alpha \end{bmatrix} = \begin{bmatrix} 0 \\ \mathbf{y} \end{bmatrix} \tag{13}$$

where $\alpha = [\alpha_1, \ldots, \alpha_L]^T$, $\mathbf{y} = [y_1, \ldots, y_L]^T$, $\mathbf{1}^T = [1, \ldots, 1] \in \mathbb{R}^{L \times L}$, $\mathbf{I} \in \mathbb{R}^{L \times L}$ is the identity matrix and $\Omega \in \mathbb{R}^{L \times L}$ is the kernel matrix.

By calculating α and b of equations in (13), the nonlinear regression model in the dual space can be obtained:

$$\mathcal{M}_{LS-SVM}(\mathbf{x}) = \sum_{i=1}^{L} \alpha_i K(\mathbf{x}_i, \mathbf{x}) + b \tag{14}$$

For a certain training set $\{\mathbf{C_{ri}}\}_{\mathbf{i=1}}^{\mathbf{N}}$, $\mathbf{C_{ri}}$ is one of the training samples consists of $\widehat{\mathbf{C}_\mathbf{r}}$ and the corresponding $\mathbf{C_m}$, by solving the equations in (13), the estimation function can be obtained:

$$\mathbf{C_m} = \sum_{i=1}^{N} \alpha_i K(\widehat{\mathbf{C}_{\mathbf{ri}}}, \widehat{\mathbf{C}_\mathbf{r}}) + b \tag{15}$$

The input $\mathbf{C_e}^*$ to the corresponding regression models and $\widehat{\mathbf{C}_\mathbf{m}}$ can be acquired. Subsequently, $\widehat{\mathbf{C}}$ can be obtained by combining $\widehat{\mathbf{C}_\mathbf{m}}$ and $\widetilde{\mathbf{C}}$.

D. IMAGE RECONSTRUCTION

The total variation (TV) method is capable of minimizing the impact of error in the measurements. The TV of an image is defined as:

$$TV(\mathbf{g}) = \sum_i \sum_j |\nabla \mathbf{g}(i, j)| \tag{16}$$

where $\mathbf{g}$ is the image matrix and $\mathbf{g}(i, j)$ is the gray value of pixel (i, j).

A general form of TV algorithm is to find $\mathbf{g}$, which satisfies

$$\arg\min_{\mathbf{g}} \left[\lambda TV(\mathbf{g}) + ||\mathbf{S} \cdot \mathbf{g} - \mathbf{C}||_2^2 \right] \tag{17}$$

where λ is the Lagrangian constant and $\mathbf{g}$ is the image obtained from the measurement set $\mathbf{C}$.

The minimization is achieved by gradient descent method. More details on the algorithm may be found in [19], [20].

III. RESULTS AND DISCUSSIONS

The proposed method is numerically tested to verify its feasibility. In addition, the recovery method has also been evaluated by the experiments using a 12-electrode ECT measurement system.

A. SIMULATIONS

The numerical simulations are carried out by using a finite element analysis (FEA) software, *i.e.* **Comsol**$^{\mathbf{TM}}$ Multi-Physics. A single plane 12-electrode ECT sensor is employed in the simulations, as illustrated in Fig. 2. The opening angle of each electrode is 27°. The outer diameter and thickness of pipe are 110 *mm* and 5 *mm*, respectively. The relative permittivity of pipe wall is 4.2. The LS-SVM MATLAB toolbox [17], is employed to train the proposed regression model. A desktop computer (Intel(R) Core(TM) i7-4720 CPU and 16.0 GB RAM) is used for the simulations and data processing.

The mathematical model of ECT sensitivity field is:

$$\nabla \cdot \varepsilon(x, y, z) \nabla \varphi(x, y, z) = 0 \tag{18}$$

where $\varepsilon(x, y, z)$ is the permittivity distribution in the sensing field and $\varphi(x, y, z)$ is the potential distribution. The relationship between capacitance and permittivity distribution is governed by:

$$\mathcal{C} = \frac{Q}{V_e} = -\frac{1}{V_e} \int_{\Omega_m} \varepsilon(x, y, z) \nabla \varphi(x, y, z) d\Omega \tag{19}$$

where V_e is the potential difference between two electrodes forming the capacitance and Ω_m is the electrode surface.

The aforementioned measurement sets serve as the training samples of regression models. These samples are clustered into 12 categories, forming 12 training sets of independent LS-SVM regression models with single layer.

In the simulations, three phantoms mimic the cross section of annular flow, core flow and stratified flow of gas-solids distributions, which are different from the training samples, as listed in column 1 in Table 2. For the boundary conditions, the potential of excitation electrode is set to 5 V, while all other electrodes are set to ground. The low and high permittivity materials are air and Perspex, respectively. The shaded parts indicate the high permittivity material.

The parameters in the simulations and experiments are set same, *i.e.* the number of categories of K-means is 12, the quantity of decision trees of RF classification is 100 and

TABLE 2. Image reconstruction results with simulation data.

# Distribution	Phantoms	Complete sets	Incomplete sets	Recovered results
1 Annular	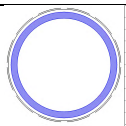	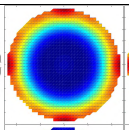	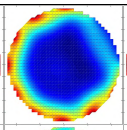	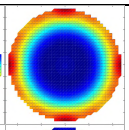
2 Core	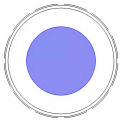	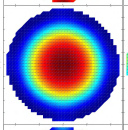	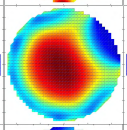	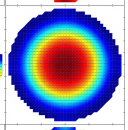
3 Stratified	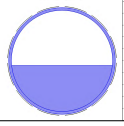	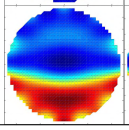	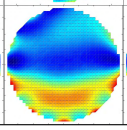	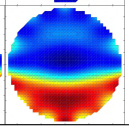

TABLE 3. Relative error with simulation imaging results.

Phantom sequence	1	2	3
Incomplete set	0.2022	0.2418	0.1682
Recovered set	0.0047	0.006	0.0227

TABLE 4. MSE (%) with simulation imaging results.

Phantom sequence	1	2	3
Incomplete set	15.81%	5.02%	4.32%
Recovered set	0.05%	0.06%	0.35%

the preset parameters of LS-SVM (γ and $\sigma 2$) are 255 and 7057.1, respectively.

It is assumed that there existed two grounded electrodes that failed to provide the correct measurements, *i.e.* the electrode 1 and 2 as indicated in Fig. 2. In this case, the number of measurements in the incomplete effective measurement sets is reduced from 66 to 45, suggesting 21 missing measurements. The images are reconstructed from the complete and incomplete measurement sets by using TV algorithm, as listed in columns 3 and 4 in Table 2, respectively. The proposed method is employed to restore the missing measurements. The reconstructed images are listed in the last column of Table 2.

The mean squared error (MSE) and relative error (ε_{img}) are employed to evaluate the imaging results, as defined by:

$$\varepsilon_{img} = \frac{||\mathbf{g}' - \mathbf{g}||_1}{||\mathbf{g}||_1} \tag{20}$$

$$MSE = \frac{||\mathbf{g}' - \mathbf{g}||_2}{||\mathbf{g}||_2} \tag{21}$$

where $\mathbf{g}'$ can be $\widehat{\mathbf{g}}$ or $\widetilde{\mathbf{g}}$, $||\cdot||_1$ and $||\cdot||_2$ denote the L1-norm and L2-norm, respectively.

In Table 2 for the phantom 1, the image obtained from the incomplete measurement set indicates that the impact of missing measurements mainly focuses on the neighborhood of the two failed electrodes. For the phantom 2, the missing measurements not only influence the image areas near the two failed electrodes, but also most of the imaging areas. For the phantom 3, the gray value decreases significantly due to the missing measurements, especially for the high permittivity part.

At the same time, it can be seen that the images obtained from the recovered measurement sets (column 5) are closer to those of complete measurement sets (column 3) in Table 2. The images calculated from the recovered and complete measurement sets demonstrate only minor differences.

The image errors, ε_{img} and MSE, of tested phantoms are shown in Table 3 and 4. It can be found that both the ε_{img} and MSE are decreased after the application of measurements recovery. However, for the phantom 3, the MSE, 0.35%, and ε_{img}, 0.0227, are slightly larger when compared with other phantoms. This is because the regression model of recovery method cannot ideally fit all the relationships between $\widehat{\mathbf{C}}'$ and $\mathbf{C_m}$.

B. EXPERIMENTS

The experiments are carried out with an ECT system that developed in Tianjin University, as illustrated in Fig. 8. The signal-to-noise ratio (SNR) is 65.0 *dB*.

As shown in Fig.9, the outer diameter and thickness of measured pipe is 110 *mm* and 5 *mm*. The length and angle of each electrode is 120 *mm* and 27°. It is assumed that the electrodes that marked in red circles are not able to provide the correct measurements. Note that there are actually two different cases of measuring failure in ECT, *i.e.* (1) the failed electrode work as a piece of grounded metal during the measurement, and (2) the failed electrodes work as a floating metal piece. Both cases have been considered in the experiments.

The experiments of gas-solids two-phase flow measurement are conducted to validate the recovery method. For the implementation, Perspex pipe and particles are used to mimic the cross-sectional of annular, slug, stratified and core of solid phase. There are 4000 training samples of regression models that collected with the system, *i.e.* by continuously changing the locations/distributions in the cross-sectional of sensor and measuring the capacitances. Among the 4000 training samples, each kind of measured components contains 1000 samples. In addition, the random noise is added to training samples, reducing SNR to 55.0 *dB* to enhance the robustness of regression model. The phantoms different from training samples for verification are listed in column 1 in Table 5. The relative permittivity of tested objects is 4.2 and the number of pixels in the imaging areas is 3228.

The phantoms 1 and 2 are tested with the case 1 caused by grounding the failed electrodes, and the phantoms 3 and 4 are tested with the case 2 caused by unplugging the signal cables of failed electrodes.

The comparison of measured value, recovered value and theoretical value of missing measurements is shown in Fig. 10. The measured value of missing measurements is set to 0 because the grounded electrodes are no longer able to acquire measurements in the case 1, while the normalized capacitance is less than 0 in the case 2. In the case 1 for the

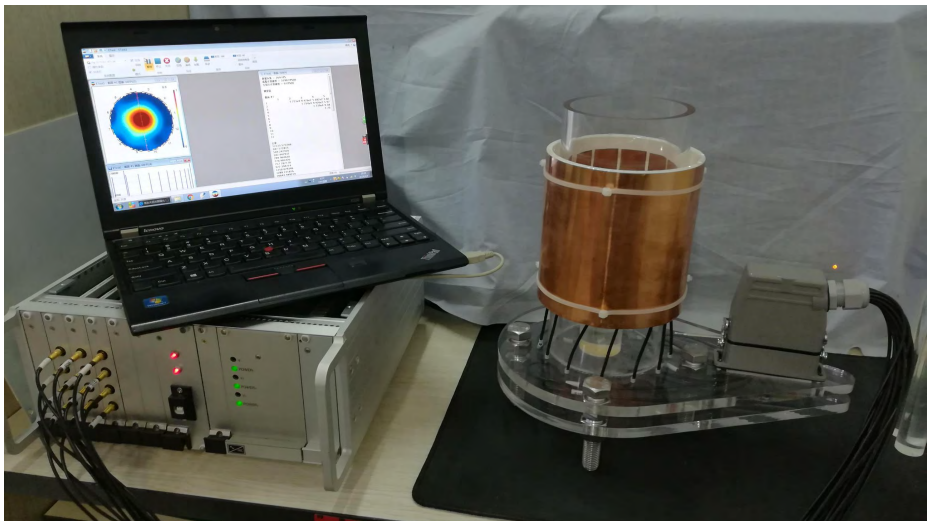

FIGURE 8. Experimental setup.

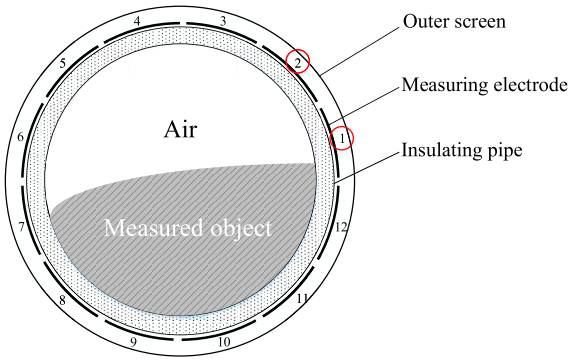

FIGURE 9. Sensor cross-sectional.

tested phantoms 1 and 2, *i.e.* in Fig. 10(a) and (b), it can be found that the missing measurements can be approximated with minor recovery error. The error is produced by regression models. In the case 2 for the tested phantoms 3 and 4, *i.e.* in Fig. 10(c) and (d), it can be found that the measurement recovery error is greater than the first case, especially for the electrode 2.

The images calculated from the complete, incomplete and recovered measurement sets are listed in column 3 $\sim$ 5 in Table 5, respectively.

In phantom 1, a Perspex pipe is positioned in center of measuring area to mimic the cross-sectional of annular flow. Its outer diameter and thickness are 80 *mm* and 5 *mm*. It can be found in the image of incomplete set that the shape of measured pipe adjacent to the failed electrodes fail to be reconstructed and the artefact is obvious. By restoring the missing measurements, the calculated image demonstrates little differences as compared with the image obtained from the complete set.

For phantom 2, a Perspex pipe of 90 *mm* in outer diameter is filled with Perspex particles and positioned on the bottom

TABLE 5. Image reconstruction results with experimental data in the condition of failed electrodes 1 and 2.

#	Phantoms Distribution	Complete sets	Incomplete sets	Recovered results
1	Annular	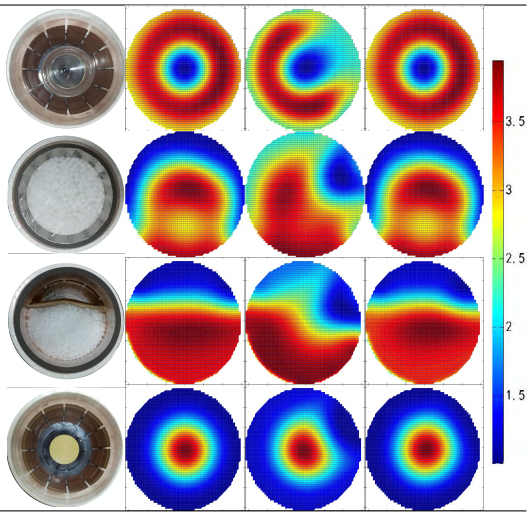		
2	Slug			
3	Stratified			
4	Core			

of the pipe to mimic the cross section of particle slug. In the image of incomplete set, the shape of slug is distorted, especially in the neighboring area of failed electrodes. In addition, the significant change can be observed from permittivity distribution of slug area. By restoring the missing measurements, the shape of solid slug has been recovered and the image shows little discrepancy with the image of complete set.

For phantom 3, Perspex particles are positioned in the lower half of the pipe imitating the cross-sectional of stratified flow. In the image of incomplete set, the boundary of dielectrics is distorted severely with obvious artefact. By recovering the missing measurements, to some extent,

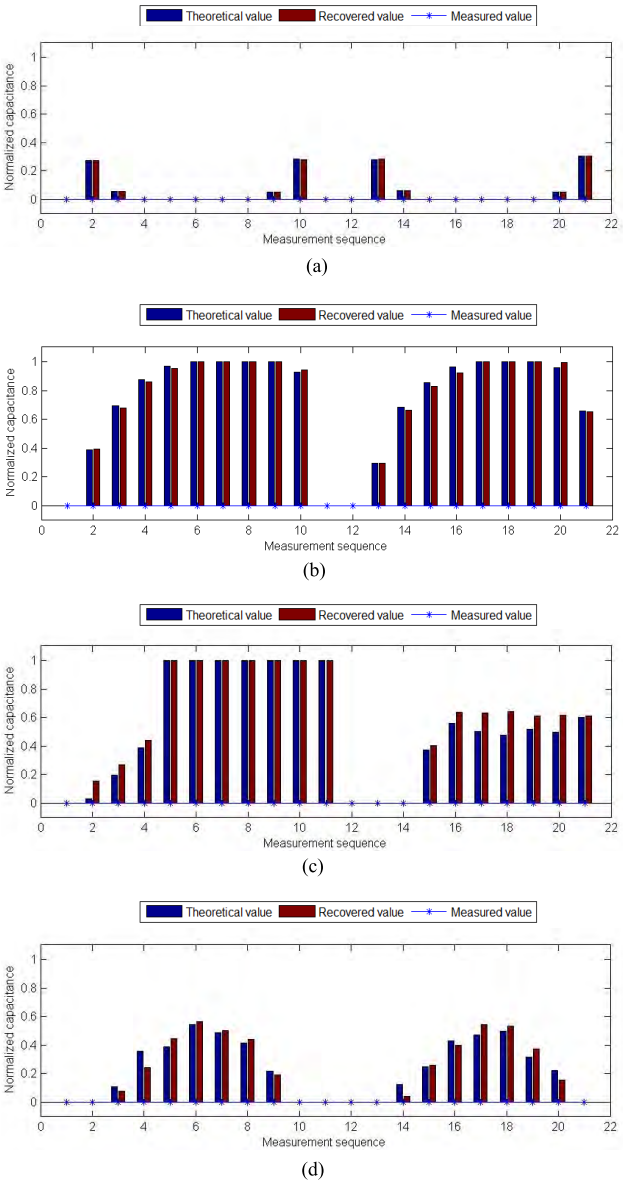

FIGURE 10. Comparisons between the actual and recovered measurements of: (a) phantom 1,(b) phantom 2, (c) phantom 3 and (d) phantom 4.

TABLE 6. Image reconstruction results with experimental data in the condition of failed electrodes 1 and 4.

# Distribution	Phantoms	Complete sets	Incomplete sets	Recovered results
1 Annular				
2 Slug				
3 Stratified				
4 Core				

TABLE 7. Image reconstruction results with experimental data in the condition of failed electrodes 1 and 7.

# Distribution	Phantoms	Complete sets	Incomplete sets	Recovered results
1 Annular				
2 Slug				
3 Stratified				
4 Core				

the image of dielectric distribution in the vicinity of failed electrodes is recovered. However, due to the measurement recovery error, the boundary next to the failed electrodes is still crooked slightly and the gray value incorrectly decreased from top to bottom of imaging areas.

For phantom 4, a Perspex rod of 40 *mm* in diameter, positioned in the center of the pipe to mimic the cross-sectional of core flow. Even though the rod positioned away from the two failed electrodes, the reconstructed object near the failed electrodes has also been distorted. By recovering the missing measurements, the distortion areas are recovered with little discrepancy compared with the image of complete set.

Note that the possible combination of failed electrodes may vary. Therefore, four typical failed conditions are selected to test the recovery method, *i.e.* the electrodes 1 and 2, 1 and 4, 1 and 7, 3 and 4.

To test the measurement recovery results in different conditions, 10-fold cross-validation method is used to divided all the samples into the training and validation samples. The calculated MSE between recovered and theoretical value of failed measurements is shown in Table 9. It can be seen that the different combinations of failed electrodes have very little impact on the performance of recovery method. However, the error increase significantly when the two failed electrodes are adjacent to each other.

The image reconstruction result in the condition of failed electrodes 1 and 4, 1 and 7, 3 and 4 are shown in Table 6, 7, and 8, respectively. In these conditions, the images near the failed electrodes are severely distorted, while the images of

TABLE 8. Image reconstruction results with experimental data in the condition of failed electrodes 3 and 4.

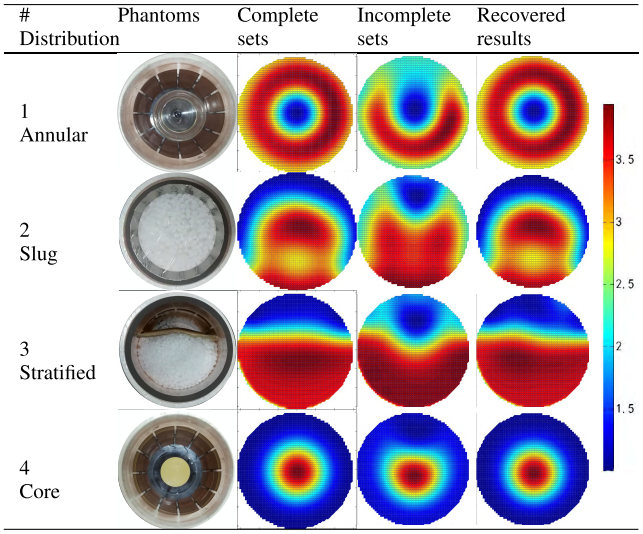

TABLE 9. MSE (%) of 10-fold cross-validation results.

Failed electrodes	1 and 2	1 and 4	1 and 7	3 and 4
	0.66%	0.32%	0.53%	0.67%

TABLE 10. Relative error of recovered and unprocessed imaging results in different conditions of failed electrodes.

Phantoms	1	2	3	4
Unprocessed C 1	0.1346	0.1379	0.2291	0.1453
Unprocessed C 2	0.1081	0.1152	0.1911	0.1126
Unprocessed C 3	0.1037	0.1145	0.2474	0.1125
Unprocessed C 4	0.1315	0.1163	0.1792	0.1472
Recovered C 1	0.0031	0.0012	0.0493	0.0298
Recovered C 2	0.0003	0.0029	0.0584	0.0212
Recovered C 3	0.0008	0.0043	0.0292	0.0325
Recovered C 4	0.0011	0.0053	0.0353	0.0164

recovered sets are approximately recovered as compared with the images of complete sets.

In the different conditions of failed electrodes, the training and test samples of recovery method need to be reorganized. However, these samples are calculated from the original samples of complete measurement sets, which can be performed automatically. The procedure of reorganizing samples for a certain condition averagely costs 0.32 second. Furthermore, the recovery procedure costs 5.3 second for 170 test samples. It means that the recovery method is able to be implemented in real-time measurement and is flexible for different conditions of failed electrodes.

The image errors, ε_{img} and *MSE*, for the different tested phantoms were calculated and listed in Table 10 and Table 11. In the tables, C 1, C 2, C 3, C 4 represent the failed electrode combinations of 1 and 2, 1 and 4, 1 and 7, 3 and 4, respectively. It can be seen that, in both cases of measurement failure

TABLE 11. MSE (%) of recovered and unprocessed imaging results in different conditions of failed electrodes.

Phantoms	1	2	3	4
Unprocessed C 1	8.98%	14.86%	21.73%	2.12%
Unprocessed C 2	3.13%	6.72%	10.39%	1.39%
Unprocessed C 3	2.44%	6.01%	21.73%	2.12%
Unprocessed C 4	8.57%	9.15%	5.35%	2.11%
Recovered C 1	0.01%	0.02%	0.24%	0.18%
Recovered C 2	0.01%	0.01%	0.99%	0.16%
Recovered C 3	0.06%	0.01%	0.29%	0.21%
Recovered C 4	0.01%	0.03%	0.39%	0.13%

and different conditions of failed electrodes, ε_{img} and *MSE* are decreased after the recovery of missing measurements. Both the ε_{img} and *MSE* between the recovered and complete measurement sets are relatively small in the first case of measurement failure and it gets greater in the second case.

The errors of image and recovered measurements could be further decreased. For the first case, it can be achieved by optimizing the regression model. And, for the second case, the recovery error is mainly caused by the measurement noise of incomplete measurement set which cannot be eliminate by the recovery method. The error may be decreased by:

(1) using a fine-tuned sensitivity matrix;

(2) utilizing the domain analysis method to remove the measurements caused by the floating electrodes;

(3) improving the robustness of recovery method.

IV. CONCLUSIONS

An incomplete measurement set recovery method has been introduced in ECT to recover the missing measurements caused by the failed electrodes or cables. The image reconstruction results may be severely influenced by the measurements that related to the failed electrodes. The prior information of sensitivity matrix and LS-SVM regression model are utilized to fit the relationship between the incomplete measurement set and missing measurements. By applying the measurement recovery method and TV algorithm, ECT system is able to obtain the imaging results that are very close to the normal conditions.

The recovery method can improve the reliability of ECT system in the harsh industrial environments. Although it is needed to prepare a large amount of training samples prior to the recovery process, it is needed to be done only once. Therefore, one does not need to pay special attention to its execution efficiency. The experiments of gas-solid two-phase flows are performed to validate the effectiveness of the method.

In the future, the method will be tested in the gas-solid flows in a pneumatic conveying processes. Furthermore, the improvement on the speed and accuracy of recovery method will be conducted. And, the case of more failed electrodes, *i.e.* 3 or more, will also be considered. The components of recovery method are flexible and the

recovery effect could be further improved by introducing the appropriate algorithms. In addition, the method can also be applied to other tomographic modalities, including electrical resistance/impedance tomography and electromagnetic tomography.

REFERENCES

[1] M. Aghbashlo, R. Sotudeh-Gharebagh, R. Zarghami, A. S. Mujumdar, and N. Mostoufi, "Measurement techniques to monitor and control fluidization quality in fluidized bed dryers: A review," *Drying Technol.*, vol. 32, no. 9, pp. 1005–1051, 2014.
[2] J. Porzuczek, "Applications of electrical capacitance tomography for research on phenomenon occurring in the fluidised bed reactors," *Chem. Process Eng.*, vol. 35, no. 4, pp. 397–408, Dec. 2014.
[3] H. Wang, W. Yang, I. Proctor, J. Taylor, A. Marr, and T. Page, "Online monitoring and flow regime identification of fluidised bed drying and granulation processes," in *Proc. IEEE Int. Workshop Imag. Syst. Techn.*, May 2009, pp. 247–252.
[4] J. Yao and M. Takei, "Application of process tomography to multiphase flow measurement in industrial and biomedical fields: A review," *IEEE Sensors J.*, vol. 17, no. 24, pp. 8196–8205, Dec. 2017.
[5] J. Liu, S. Liu, W. Zhou, Y. Kang, and H. I. Schlaberg, "Flame detection on swirl burner using ECT with dynamic reconstruction algorithm based on the split Bregman iteration," *IEEE Sensors J.*, vol. 17, no. 22, pp. 7290–7297, Nov. 2017.
[6] Q. Chen, Y. Jia, X. Mao, and Y. Ju, "Direct measurements of permittivity of plasma-assisted combustion using electrical capacitance tomography," *IEEE Trans. Plasma Sci.*, vol. 44, no. 12, pp. 3009–3016, Dec. 2016.
[7] Q. Xue, H. Wang, C. Yang, and Z. Cui, "Change-point-detection-based method for solid velocity measurement using twin-plane electrical capacitance tomography," in *Proc. Instrum. Meas. Technol. Conf.*, May 2012, pp. 2414–2418.
[8] V. Mosorov, "Flow pattern tracing for mass flow rate measurement in pneumatic conveying using twin plane electrical capacitance tomography," *Part. Part. Syst. Characterization*, vol. 25, no. 3, pp. 259–265, 2010.
[9] P. L. Roth, "Missing data: A conceptual review for applied psychologists," *Pers. Psychol.*, vol. 47, no. 3, pp. 537–560, 2010.
[10] E. Castillo, N. Sánchezmaroño, A. Alonsobetanzos, and C. Castillo, "Recovering missing data with functional and Bayesian networks," in *Proc. Int. Work-Conf. Artif. Natural Neural Netw., Artif. Neural Nets Problem Solving Methods (Iwann)*, Menorca, Spain, Jun. 2003, pp. 489–496.
[11] A. Raheja and A. P. Dhawan, "Multiresolution expectation maximization reconstruction algorithm for positron emission tomography using wavelet processing," in *Proc. 20th Annu. Int. Conf. IEEE Eng. Med. Biol. Soc.*, vol. 2, Oct. 1998, pp. 759–762.
[12] E. Rabinovich and H. Kalman, "Flow regime diagram for vertical pneumatic conveying and fluidized bed systems," *Powder Technol.*, vol. 207, nos. 1–3, pp. 119–133, 2011.
[13] T. Dyakowski, R. B. Edwards, C. G. Xie, and R. A. Williams, "Application of capacitance tomography to gas-solid flows," *Chem. Eng. Sci.*, vol. 52, no. 13, pp. 2099–2110, 1997.
[14] D. Bing, W. Warsito, and L. S. Fan, "Bed nonhomogeneity in turbulent gas-solid fluidization," *AIChE J.*, vol. 49, no. 5, pp. 1109–1126, 2010.
[15] A. K. Jain and R. C. Dubes, "Algorithms for clustering data," *Technometrics*, vol. 32, no. 2, pp. 227–229, 1988.
[16] H. Wang and D. Hu, "Comparison of SVM and LS-SVM for regression," in *Proc. Int. Conf. Neural Netw. Brain*, Oct. 2006, pp. 279–283.
[17] J. A. K. Suykens, T. V. Gestel, J. D. Brabanter, B. D. Moor, and J. Vandewalle, *Least Squares Support Vector Machines*. Singapore: World Scientific, 2002, pp. 21–23.
[18] R. Trinchero, M. Larbi, H. Torun, F. G. Canavero, and M. Swaminathan, "Machine learning and uncertainty quantification for surrogate models of integrated devices with a large number of parameters," *IEEE Access*, vol. 7, pp. 4056–4066, 2018.
[19] Z. Cui, Q. Wang, Q. Xue, W. Fan, L. Zhang, Z. Cao, B. Sun, H. Wang, and W. Yang, "A review on image reconstruction algorithms for electrical capacitance/resistance tomography," *Sensor Rev.*, vol. 36, no. 4, pp. 429–445, 2016.
[20] S. Ahn, S. M. Kim, J. Son, D. S. Lee, and J. S. Lee, "Gap compensation during PET image reconstruction by constrained, total variation minimization," *Med. Phys.*, vol. 39, no. 2, pp. 589–602, 2012.

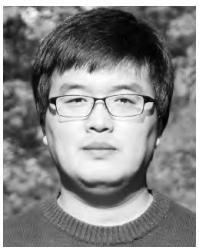

ZIQIANG CUI (M'13) received the M.Sc. and Ph.D. degrees from Tianjin University, China, in 2007 and 2009, respectively, where he is currently an Associate Professor with the School of Electrical and Information Engineering. His current research interests include electrical tomography instrumentation, signal processing, sensor design, and multi-phase flow measurement.

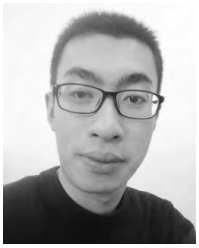

ZIHAN XIA received the B.Sc. degree from North China Electric Power University, China, in 2017. He is currently pursuing the master's degree with the School of Electrical and Information Engineering, Tianjin University. His current research interests include process tomography, artificial intelligence, and multi-phase flow measurement.

HUAXIANG WANG (SM'06) received the degree from Tianjin University, China, where he is currently a Professor with the School of Electrical and Information Engineering. His major research interests include sensing techniques and information processing, process parameter detection and control systems, and intelligent instrumentations.